Applied Catalysis B: Environmental 331 (2023) 122710

Contents lists available at ScienceDirect

Applied Catalysis B: Environmental

journal homepage: www.elsevier.com/locate/apcatb

Atomic ruthenium modification of nickel-cobalt alloy for enhanced alkaline hydrogen evolution

Liuqing Li [a,b,1], Haifa Qiu [a,1], Yanping Zhu [a,*], Gao Chen [a], Sixuan She [a], Xuyun Guo [a], Hao Li [a], Tiancheng Liu [a], Zezhou Lin [a], Hanmo Zhou [a,c], Ye Zhu [a], Ming Yang [a], Baomin Xu [b,*], Haitao Huang [a,*]

[a] Department of Applied Physics, The Hong Kong Polytechnic University, Hung Hom, Kowloon, Hong Kong, China
[b] Department of Materials Science and Engineering, Southern University of Science and Technology, Nanshan District, Shenzhen, Guangdong, China
[c] Faculty of System Design and Intelligent Manufacturing, Southern University of Science and Technology, Nanshan District, Shenzhen, Guangdong, China

ARTICLE INFO

Keywords:
Hydrogen evolution reaction
Ru-decorated catalyst
Density functional theory
Water splitting
Synergistic effects

ABSTRACT

Density functional theory (DFT) is used to predict the behavior of ruthenium-doped nickel cobalt alloy in the alkaline hydrogen evolution reaction (HER). According to DFT calculation, a synergistic effect at the Ru-Ni/Co interface is generated to accelerate water dissociation and optimize the adsorption-desorption energetics toward the H intermediate. However, excessive Ru introduction will lead to over-strong hydrogen adsorption on the catalyst surface, thus limiting H_2 release. As a proof of concept, we design a series of $NiCoRu_x$/SP, among which the optimized $NiCoRu_{0.2}$/SP electrocatalyst achieves an overpotential of 59 mV at 10 mA cm^{-2}, while excessive Ru incorporation ($NiCoRu_{0.3}$/SP) diminishes the HER activity. X-ray absorption spectroscopy and other characterizations further confirm that the interface-induced electron transfer from atomic Ru to its surrounding Ni/Co, and the activity degradation caused by excessive Ru incorporation is attributed to the generation of Ru cluster that sacrifices the interface between Ru atom and Ni/Co.

1. Introduction

Hydrogen evolution reaction (HER) plays an indispensable role in sustainable and green hydrogen energy production from water splitting [1–4]. The sluggish electron-transfer kinetics of oxygen evolution reaction in acidic media and the expensive proton exchange membranes limit the application of water splitting in acidic electrolytes [5–7]. Fortunately, these issues can be solved when this reaction is driven in an alkaline environment, where the HER is believed to consist of two pathways: Volmer/Heyrovsky pathway or Volmer/Tafel pathway (∗ is the active site) [8–10].

$$H_2O + * + e^- \rightarrow *H + OH^- (Volmer) \quad (1)$$

$$*H + H_2O + e^- \rightarrow H_2 + OH^- (Heyrovsky) \quad (2)$$

$$2*H \rightarrow H_2 (Tafel) \quad (3)$$

Platinum (Pt)-based materials have served as the state-of-art electrocatalysts for alkaline HER. However, its high price and scarce reserves urge scientists to find alternative catalysts. Ruthenium (Ru), an element with 1/3 price of Pt but a similar property has been widely investigated as an electrocatalyst for HER [11–13]. Up to now, encouraging progress has been made by decorating transition metal catalysts, such as metal alloys [14–16], oxides [17,18], hydroxides [19,20], phosphides [21,22], chalcogenides [23], etc. with Ru for enhanced HER performance. In theory, due to the much higher catalytic activity of Ru than the transition metal counterparts, the HER performance of the Ru-decorated catalyst should be continuously improved with the increase of Ru content, which, however, is inconsistent with the experimental facts. Generally, there is an optimal value for the amount of Ru, beyond which the HER performance would decline. In most reports, the optimal amount was obtained simply from the electrochemical evaluations, leaving the underlying reasons for the excessive-doping-induced activity degradation untold. Therefore, efforts are still needed to unveil the effect of doping amount on the structure and catalytic performance of the materials.

* Corresponding authors.
E-mail addresses: yan-ping.zhu@polyu.edu.hk (Y. Zhu), xubm@sustech.edu.cn (B. Xu), aphhuang@polyu.edu.hk (H. Huang).
[1] These authors contribute equally to this work.

https://doi.org/10.1016/j.apcatb.2023.122710
Received 2 January 2023; Received in revised form 28 March 2023; Accepted 29 March 2023
Available online 30 March 2023

For a long time, trial and error is the most frequently used strategy in developing new catalyst materials for electrochemical reactions. Great efforts are needed in selecting raw materials, determining the mole ratio of reactants and optimizing reaction conditions (time and temperature). Moreover, even if satisfactory performance can be obtained for some catalysts, their complicated synthesis procedures may make them not feasible in practical applications. Theoretical computing based on density functional theory (DFT) has been extensively applied in the field of electrocatalysis. By dealing with adsorption energies, reaction thermodynamics and activation barriers, it can accurately identify the active species of solid catalysts and help uncover the origin of the electrocatalytic activity of electrode materials. More significantly, predicting the activity of potential catalysts is another important function of the DFT calculation, which will provide convincing design principles for guiding the development of novel electrocatalysts. Also, this will greatly save the time and energy involved in trial and error. For instance, Jiao et al. built seventy-two possible HER active sites according to 15 models to find the best sites for HER for the heteroatom-doped graphene model [24]. The subsequent proof-of-concept experiments were conducted with results agreeing well with the predicted trend. Inspired by this, herein, guided by the DFT study relating to the effect of Ru doping on the HER performance of NiCo alloy, the atomic Ru doped NiCo alloy dispersed on Super P carbon substrate ($NiCoRu_n$/SP) was subtly designed and facilely synthesized as robust electrocatalysts for HER. DFT calculation suggested that introducing Ru into the NiCo matrix would generate a synergistic effect at the Ru-Ni/Co interface, which not only accelerates the rate of water dissociation but also optimizes the adsorption-desorption energetic toward the H intermediate, enhancing the alkaline HER activity. But excessive Ru introduction would lead to over-strong hydrogen adsorption on the catalyst surface, which restricts H_2 release and thus decreases the activity. As a proof of concept, from electrochemical results, the optimized $NiCoRu_{0.2}$/SP electrocatalyst was revealed to achieve 10 mA cm^{-2} at a low overpotential of 59 mV in alkaline HER, while excessive Ru incorporation ($NiCoRu_{0.3}$/SP) does diminish the HER activity in turn. Results of X-ray absorption spectroscopy (XAS) and other characterizations further determined that the interface-induced electron transfer from atomic Ru to its surrounding Ni/Co, and the activity degradation caused by excessive Ru incorporation was attributed to the generation of Ru cluster that sacrificed the interface between Ru atom and Ni/Co.

2. Results and discussion

DFT calculations were first carried out on the NiCo alloy, metal Ru, and a series of $NiCoRu_n$ (n = 1, 2, 3, 4) electrodes with a focus on unveiling the effect of Ru doping on the HER activity to guide the following experimental verification. The mole ratio of Ni to Co was fixed as 1:1 and the n value ranging from 1 to 4 referred to the gradually increased amount of Ru in the NiCo matrix, rather than the exact moles of Ru. Fig. S1 and Fig. S2 displayed the established catalyst models of the catalysts. Obviously, the $NiCoRu_n$ catalysts varied in their Ru content at the surface, and for the $NiCoRu_4$ model, the surface of NiCo alloy was fully covered with Ru atoms to serve for the "largest amount of Ru" case. In terms of DFT calculations, HER in alkaline environment involves some key steps including the adsorption of the H_2O molecules on the catalyst surface, water activation to transition state, dissociating H_2O into hydroxyl group (OH^-) and H apart, hydrogen adsorption after OH^- detaching from the surface, and finally the desorption of H_2 after the combination of hydrogen intermediates (H_{ads}). Generally, the dissociation of water is considered as a key rate-determining step in alkaline HER. The kinetic energy barrier of each step for the six electrode materials during HER is displayed in Fig. 1. The small water adsorption energies of all catalysts indicated the easy initiation of the Volmer step on these six structures. The energy barrier for breaking the OH-H bond in water (ΔG_B) is 0.70 eV on the NiCo surface. Such a large energy barrier would greatly hinder the dissociation of water to H_{ads}. Strikingly, after introducing Ru into the NiCo matrix, the ΔG_B value of the $NiCoRu_1$ catalyst is decreased to 0.64 eV. With the increase of doping amount, the dissociation barrier continues to reduce from 0.55 eV for the $NiCoRu_2$ to 0.30 eV for the $NiCoRu_4$. These indicate that the sluggish Volmer process could be accelerated after incorporating Ru into the NiCo alloy, and the more Ru the doping amount, the lower the energy barrier for the

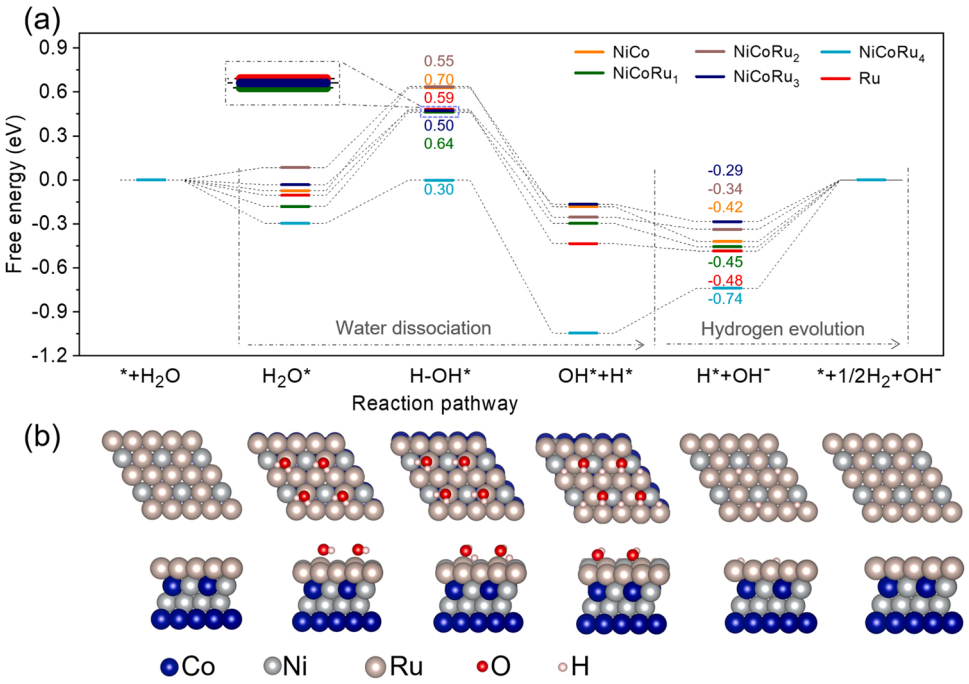

Fig. 1. (a) Gibbs free energy diagram of HER on various surfaces along the pathway including water dissociation and hydrogen desorption.ΔG_{H*} ΔG_B (b) Atomic configurations on the surface of $NiCoRu_3$, corresponding to the pristine $NiCoRu_3$ before adsorption, the initial state, transition state and final state of water dissociation as well as the hydrogen adsorption intermediate state, respectively.

water dissociation. It is worth to be noted that the ΔG_B value of the pure Ru is not the lowest among all the catalysts (0.59 eV), which demonstrates that when dissociating water molecules, the strong coupling of the two phases would create a synergistic effect between Ru and NiCo. Subsequently, every catalyst undergoes a thermodynamically downhill pathway, revealing that the hydroxyl group is less likely to adhere to the catalyst surface site and block subsequent reactions. Then it comes to the hydrogen adsorption on the catalyst surface. According to the classic Sabatier principle, the adsorption and desorption of hydrogen on the catalyst surface should be neither too strong nor too weak. From a thermodynamic perspective, the Gibbs free energy change of hydrogen adsorption (ΔG_{H*}) should be as close to zero as possible for an ideal HER catalyst [25]. We calculated the ΔG_{H*} on each catalyst surface. With the increase of Ru amount from $NiCoRu_1$ to $NiCoRu_3$, the hydrogen-binding energy gradually approaches the optimized value. However, the $NiCoRu_4$ with fully covered Ru atoms on the surface shows a much larger ΔG_{H*} than the other three NiCoRu catalysts, which would significantly suppress the desorption of H_{ads} and H_2 production would thus be hindered. Based on the above analysis, some critical information can be obtained. First, introducing Ru into the NiCo matrix would create a synergistic effect at the Ru-Ni/Co interface, which not only accelerates the rate of water dissociation but also optimizes the adsorption-desorption energy toward the H intermediate, enhancing alkaline HER activity. Second, there is an optimal value for the Ru doping amount, rather than the more the better. Excessive Ru introduction would sacrifice the interfacial contact between NiCo and Ru atom due to the tendency to form Ru clusters, leading to over-strong hydrogen adsorption on the catalyst surface, which is not beneficial for the H_2 release, thus reducing the HER activity.

As a proof-of-concept, we designed a series of $NiCoRu_x$/SP ($x = 0.05$, 0.1, 0.2 and 0.3) nanocomposites to verify the above simulation results, where x is denoted the mole ratio between Ru and Ni (or Co) with Ni and Co having the same mole ratio. The typical synthesis procedure is shown schematically in Fig. 2. In the first step, the conductive carbon black Super P was immersed into an aqueous solution containing Ni^{2+}, Co^{2+} and Ru^{3+}, through which the mixed metal salt would be uniformly coated on the SP substrate. During the subsequent low-temperature nucleation process, the metal salt converted to $NiCoRu_x$ alloy nanoparticles and the $NiCoRu_x$ alloy supported on SP substrate was thus facilely obtained. Room-temperature X-ray diffraction (XRD) was first employed to identify the phase structure of the as-obtained composite materials. As revealed in Fig. 3**a**, for the pristine NiCo/SP catalyst, the strong diffraction peak located at 25° corresponds to the (002) plane of the standard carbon structure. The other diffraction peaks positioned at 44°, 52° and 76° can be unambiguously indexed based on the (111), (200) and (220) planes of NiCo alloy phase (JCPDS no. 15–0806), respectively. After the introduction of the guest Ru atoms, the new diffraction pattern of the representative $NiCoRu_{0.2}$/SP sample overlaps satisfactorily with that of the NiCo/SP, but with a slightly negative peak shift. No additional peaks associated with Ru meal or oxides are observed. This indicates the successful doping of Ru metal into the NiCo alloy lattice. Moreover, XRD patterns of the other three Ru-doped samples ($NiCoRu_{0.05}$/SP, $NiCoRu_{0.1}$/SP and $NiCoRu_{0.3}$/SP) are consistent with that of the $NiCoRu_{0.2}$/SP (Fig. S3). The general morphology and textural details of the as-prepared catalysts were investigated by the field-emission scanning electron microscopy (FESEM) and transmission electron microscopy (TEM). Similar to the SP sample (Fig. S4a), both NiCo/SP (Fig. S4b) and $NiCoRu_{0.2}$/SP (Fig. 3**b**) samples showed a very fluffy nature. No other smaller nanoparticles were detected, so TEM measurements were needed to further study the microstructure. As expected, the TEM image of the NiCo/SP material shows high contrast between light and dark. Numerous dark nanoparticles sized 5–10 nm are uniformly distributed (Fig. S5a), suggesting the nanosized NiCo alloy particles. In comparison, the light gray area is characteristic of the SP substrate. The representative high-resolution transmission electron microscope (HRTEM) image in Fig. S5b gives clear lattice spacing of 0.21 nm, which agrees well with the (111) plane of the cubic NiCo alloy. In addition, the corresponding energy disperses spectrum (EDS) elemental mapping analysis evidently indicates the homogeneous distribution of Ni and Co in the selected region (Fig. S5c-f). After implanting Ru atoms into the NiCo lattice, no significant changes took place in particle size or particle quantity for the $NiCoRu_{0.2}$/SP sample (Fig. 3**c**), and the element mapping demonstrated the uniform distribution of Ru across the whole NiCo particle (Fig. 3**d-f**). The mapping images of O show a hollow distribution of oxygen (Figs. S5e and 3**g**), indicating the superficial oxidization of the particle. Interestingly, the introduction of Ru atoms creates rich lattice distortion (Fig. 3**h** and **i**). Generally, as a consequence of stripping away atoms from an alloy or introducing heteroatoms into a metal matrix, the metal lattice could distort and affect the property of the composite. According to previous studies [26–29], the lattice strain might positively shift the D-band center towards the Fermi level, causing enhanced adsorption interaction with reaction intermediates and promoting electrocatalytic activity. Corresponding TEM and HRTEM images of the $NiCoRu_{0.05}$/SP, $NiCoRu_{0.1}$/SP and $NiCoRu_{0.3}$/SP shown in Fig. S6 reveal that the Ru doping amount has little influence on the particle size or the crystalline structure. N_2 adsorption/desorption isotherms tests were conducted to further investigate the pore structural property of the $NiCoRu_{0.2}$/SP sample. A typical type IV isotherm with an H_3 hysteresis loop can be observed (Fig. S7), which is characteristic of a mesoporous structured material. After calculation, the composite material possessed a Brunauer-Emmett-Teller (BET) specific surface area of 55.79 $m^2\ g^{-1}$ and a pore volume of 0.25 $m^3\ g^{-1}$. Such microstructure with a large surface area and rich pores is expected to expose more active sites and allow easy penetration of liquid electrolytes during catalyzing the HER.

The electrochemical performance of the $NiCoRu_x$/SP catalysts toward HER was assessed in the 1 M KOH electrolyte using a three-electrode configuration. For comparison, blank SP, NiCo/SP, Ru/SP and commercial 20 wt% Pt/C electrodes also have been evaluated under the same condition. The typical polarization curves (after IR correction) are displayed in Fig. 4**a**. The commercial Pt/C electrode demonstrates highly active HER performance with the lowest onset overpotential and

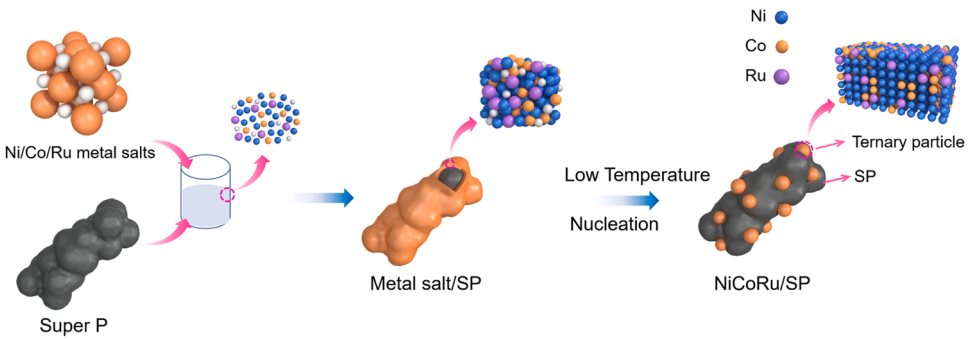

Fig. 2. Schematic illustration for synthesizing NiCoRu/SP.

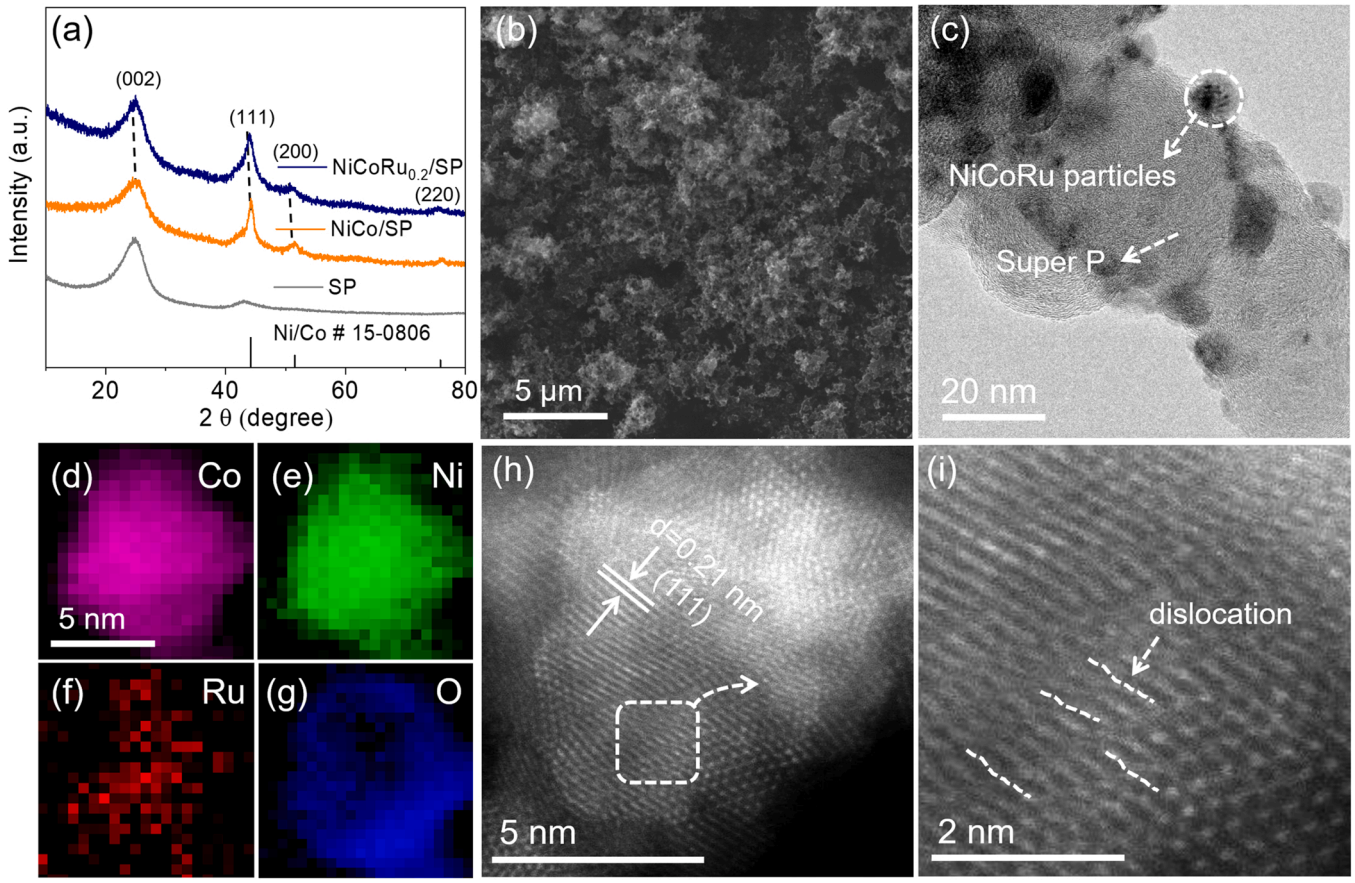

Fig. 3. XRD curves of SP, NiCo/SP and $NiCoRu_{0.2}$/SP. (b) SEM image of $NiCoRu_{0.2}$/SP. (c) TEM image of $NiCoRu_{0.2}$/SP. (d), (e), (f) and (g) are the mapping images of a circled particle in (c). (h) The Spherical Aberration Corrected TEM of a NiCoRu particle and (i) the enlarged view marked in (h).

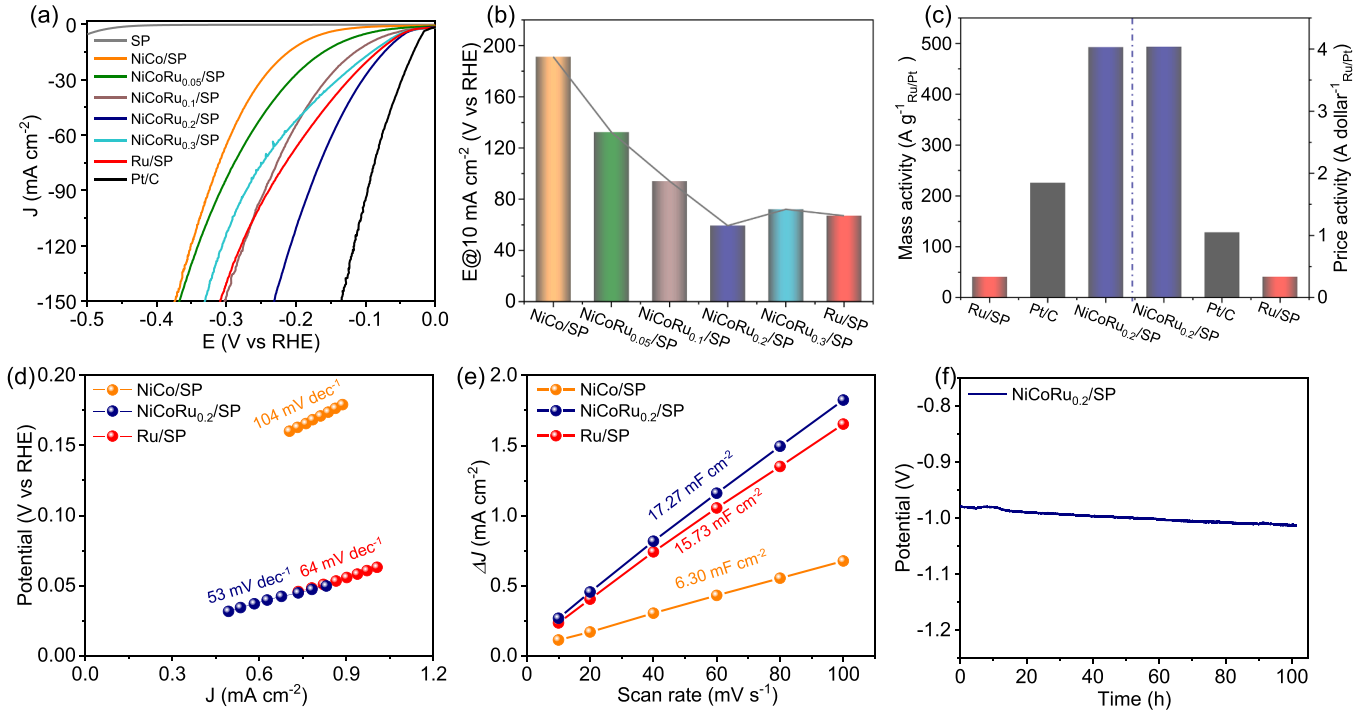

Fig. 4. Electrocatalytic evaluation. (a) Linear sweep voltammetry (LSV) curves of SP, NiCo/SP, $NiCoRu_x$/SP (x = 0.05, 0.1, 0.2, 0.3), Ru/SP and Pt/SP measured at 5 mV s^{-1} in 1 M KOH aqueous solution and (b) their corresponding overpotential at 10 mA cm^{-2}. (c) mass activity and price activity at 50 mV, (d) Tafel slopes and (e) ECSA curves of NiCo/SP, $NiCoRu_{0.2}$/SP and Ru/SP. (f) Chronopotentiometric curve of HER with a constant current density of 10 mA cm^{-2}.

an overpotential of only 25 mV to reach 10 mA cm^{-2} (η_{10}), which is consistent with the previous studies [30,31]. The NiCo/SP catalyst shows a much lower onset potential (100 mV) and smaller η_{10} value (191 mV) compared to the blank SP catalyst (onset potential of 390 mV, η_{10} = 522 mV), suggesting that the NiCo alloy rather than the carbon substrate acts as the active sites during the HER in this study. However, after introducing a small quantity of Ru atoms into the NiCo alloy, the $NiCoRu_{0.05}$/SP catalyst presents a dramatically decreased onset potential of 60 mV and a reduced overpotential of 132 mV to drive 10 mA cm^{-2}. It is noteworthy that the η_{10} values of the $NiCoRu_x$/SP catalysts followed a "decrease-increase" trend with increasing the Ru content (Fig. 4**b**), and the best $NiCoRu_{0.2}$/SP electrode needs an overpotential of only 59 mV to reach 10 mA cm^{-2}, which outperforms most of the Ru-based HER catalysts in alkaline media [32–36]. These results agree well with the above DFT simulations that introducing Ru into the NiCo matrix would significantly accelerate the HER rate while excessive Ru incorporation would sacrifice the activity in turn. It is also worth to be noted that the catalytic performance of the $NiCoRu_{0.2}$/SP electrode exceeds that of the Ru/SP containing the same Ru content, which indicates a synergistic effect between NiCo alloy and the implanted Ru atom during catalyzing the HER. Fig. 4**c** plots the mass activity (normalized to Ru/Pt loading) and price activity (normalized to price) of the samples at an overpotential of 50 mV. The $NiCoRu_{0.2}$/SP electrode delivers a mass activity of 492.50 A g^{-1}, which is 2 and 12 times that of the Pt/C and Ru/SP catalysts, respectively. With respect to the price activity, the $NiCoRu_{0.2}$/SP electrode achieves 4.04 A $dollar^{-1}$ under the overpotential of 50 mV, which is 4 and 12 times that of the Pt/C (1.05 A $dollar^{-1}$) and Ru/SP (0.33 A $dollar^{-1}$) catalyst, respectively. These results further demonstrate the superior activity and low cost of the as-prepared $NiCoRu_{0.2}$/SP catalyst.

Tafel plots were derived from the polarization curves to gain insights into the kinetics of the electrodes. As revealed in Fig. 4**d**, a Tafel slope of 53 mV dec^{-1} is obtained for the $NiCoRu_{0.2}$/SP catalyst, which is lower than that of the NiCo/SP (104 mV dec^{-1}) and Ru/SP (64 mV dec^{-1}) catalysts. A smaller Tafel slope is typically a sign of an efficient catalyst. Meanwhile, according to the three principle steps (Volmer step, 120 mV dec^{-1}, Heyrovsky step, 40 mV dec^{-1}, Tafel step, 30 mV dec^{-1}) involved in HER, the hydrogen evolution on the $NiCoRu_{0.2}$/SP electrode probably proceeded via a Volmer-Heyrovsky mechanism, where the electrochemical desorption is the rate-determining step. Further, we compared the electrochemically active surface area (ECSA) of each catalyst, which was determined by the capacitance measurement (Fig. 4**e**). It was found that the $NiCoRu_{0.2}$/SP sample gives the largest C_{dl} among the three catalysts, demonstrating the highest electrochemical surface area (Fig. S8). Figs. S9a and S9b show the polarization curves of the three catalysts after normalizing by ECSA and BET, respectively. Obviously, the $NiCoRu_{0.2}$/SP electrode still exhibits the best HER activity. This indicates the improvement in intrinsic activity after Ru introduction. Long-term stability is another critical criterion for a satisfactory catalyst. A chronopotentiometry curve for the $NiCoRu_{0.2}$/SP electrode under the fixed current density of 10 mA cm^{-2} was collected to validate that the applied potential remained identical for 100 h at least, demonstrating the robust stability of the $NiCoRu_{0.2}$/SP catalyst (Fig. 4**f**). In the corresponding TEM and HRTEM images of the post-HER electrode, the particle size is the same as that of the as-prepared catalyst (Fig. S10a), and the crystal lattice can be clearly observed (Fig. S10b). The amorphous layer observed on the particle could be nafion that was added during electrode preparation [37,38].

Finally, X-ray photoelectron spectroscopy (XPS) and XAS were performed to analyze the surface chemical state of the catalysts. Fig. 5**a** shows the high-resolution Ni 2p XPS spectra of the $NiCoRu_{0.2}$/SP and NiCo/SP catalysts. Two distinct peaks located at 872.10 and 854.21 eV of the NiCo/SP are characteristic of metallic Ni. The other two peaks at 873.53 and 855.51 eV emerged as Ni^{x+} $2p_{1/2}$ and Ni^{x+} $2p_{3/2}$, respectively, accompanied by two satellite peaks, which is due to the surface oxidation during the XPS measurement [39]. Although the XPS results indicate the surface oxidative condition of the catalyst, they do not necessarily represent the oxidation state of the material under the HER bias in solution. Actually, during the electro-derived reduction process, those oxidized species would be reduced, exposing the metallic NiCoRu

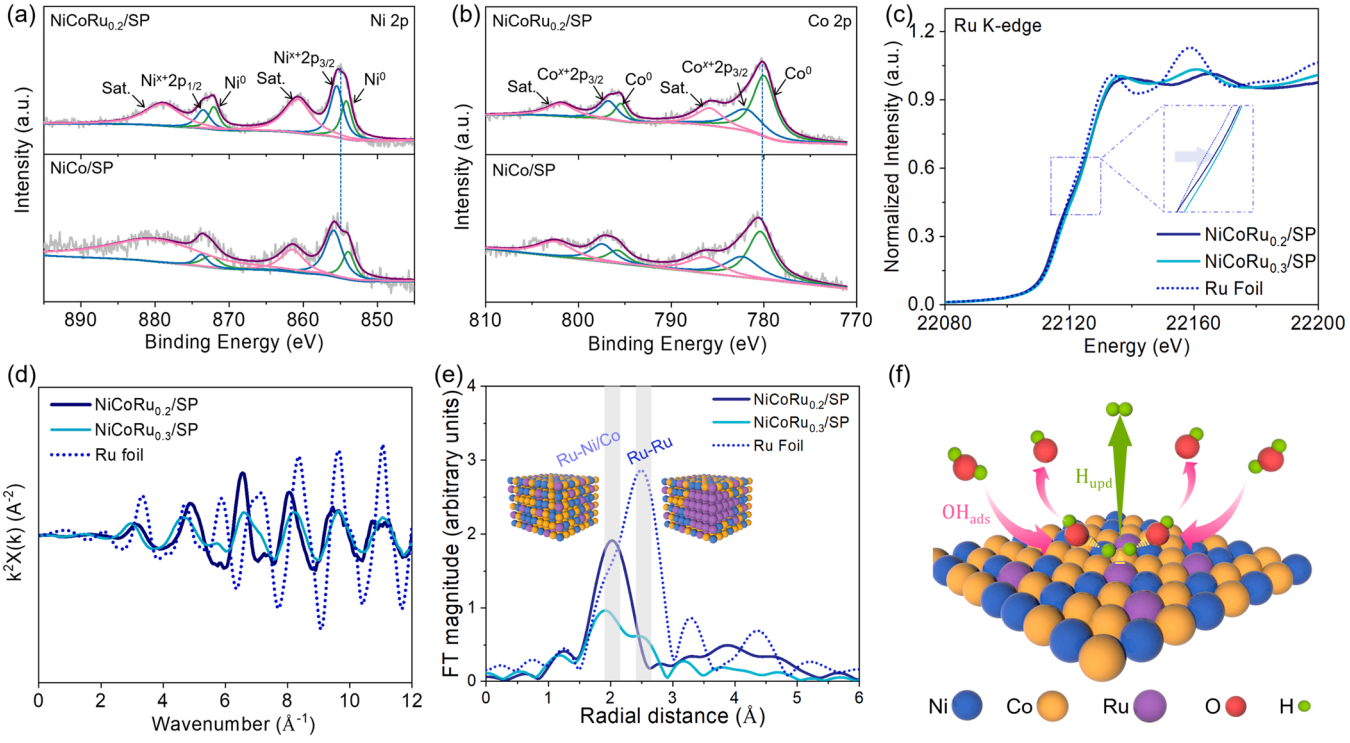

Fig. 5. (a) Ni 2p and (b) Co 2p XPS spectra for NiCo/SP and $NiCoRu_{0.2}$/SP. (c) Ru K-edge XANES spectroscopy and (d) FT-EXAFS K-space spectra and (e) FT-EXAFS R-space spectra of $NiCoRu_{0.2}$/SP, $NiCoRu_{0.3}$/SP and Ru Foil. (f) scheme for water dissociation and hydrogen evolution on the surface of $NiCoRu_{0.2}$/SP.

alloy to participate in the HER [10,40–43]. After incorporating Ru into the NiCo alloy, the intensity of metallic Ni is significantly enhanced, and the Ni 2p peaks of the $NiCoRu_{0.2}$/SP show a negative shift compared to that of the NiCo/SP catalyst, indicating the reduced oxidation state of Ni. Similar to the condition of Ni, after doping Ru, the oxidation state of Co in the $NiCoRu_{0.2}$/SP also decreased (Fig. 5**b**). Moreover, the Ru 3p spectrum for the $NiCoRu_{0.2}$/SP sample gave a negative shift compared with the pure metal Ru/SP (Fig. S11). These results suggest a strong electronic interaction between Ru and NiCo alloy, leading to electron transition from Ru to its surrounding Ni/Co. XPS spectra of the electrode material after the stability test revealed similar chemical states of Ru, Ni and Co with that of the as-prepared catalyst, demonstrating the good affordability of $NiCoRu_{0.2}$/SP in long-term operation (Fig. S12).

To gain more insights into the electronic and geometric structure of the catalysts, Ru K-edge X-ray absorption near edge structure (XANES) spectroscopy for the as-prepared $NiCoRu_{0.2}$/SP and $NiCoRu_{0.3}$/SP samples and Ru foil reference were collected as displayed in Fig. 5**c**. It can be observed that the white line of the two catalysts shift to higher energy than the metal Ru, which can be correlated with slight oxidation and is in accordance with the observations from XPS. Fig. 5**d** shows the corresponding Fourier-transformed extended X-ray absorption fine structure (FT-EXAFS) K-space spectra of the samples. The Ru foil has a distinct K-space feature from the other two catalysts. From the EXAFS R-space spectra (Fig. 5**e**), the dominant peak at around 2 Å for the $NiCoRu_{0.2}$/SP is attributed to the coordinated shell of the Ru-Ni/Co path, while the presence of metallic Ru or Ru oxides is excluded. This demonstrates the atomic dispersion of Ru in the NiCo alloy matrix. However, for the $NiCoRu_{0.3}$/SP sample with more Ru incorporation, besides the Ru-Ni/Co path, a new scattering contribution from Ru-Ru at around 2.5 Å can be observed, suggesting the co-existence of single atoms and clusters of Ru in the $NiCoRu_{0.3}$/SP catalyst. Based on the above results that introducing Ru into the NiCo matrix would generate a synergistic effect at the Ru-Ni/Co interface and the inferior activity of $NiCoRu_{0.3}$/SP electrode than that of $NiCoRu_{0.2}$/SP, it can be inferred that the generation of Ru cluster from excessive Ru incorporation would sacrifice the interface between Ru atom and Ni/Co, pulling down the efficiency of water dissociation and hydrogen release, thus degrading the HER activity (Fig. 5**f**).

3. Conclusion

In conclusion, computational simulation has been successfully used in predicting the activity of potential catalysts when they catalyze the alkaline HER. With the help of DFT calculations, the underlying mechanism for the enhanced HER activity of NiCo alloy by Ru incorporation as well as the performance degradation of excessive doping have been thoroughly illustrated. Experimentally, atomic Ru-doped NiCo alloy supported on SP substrate has been demonstrated to perform outstanding HER activity as well as robust stability. This work opens new avenues for developing active electrocatalysts in the field of electrocatalysis.

CRediT authorship contribution statement

Liuqing Li: Conceptualization, Data curation, Investigation, Formal analysis, Writing – original draft. **Haifa Qiu:** Theoretical calculation, Writing. **Yanping Zhu:** Writing – review & editing, Project administration. **Gao Chen:** Validation. **Sixuan She:** Validation. **Xuyun Guo:** Validation, Formal analysis. **Hao Li:** Resources. **Tiancheng Liu:** Resources. **Zezhou Lin:** Visualization. **Hanmo Zhou:** Validation. **Ye Zhu:** Resources. **Ming Yang:** Resources. **Baomin Xu:** Writing – review & editing, Funding acquisition, Supervision. **Haitao Huang:** Conceptualization, Writing – review & editing, Funding acquisition, Supervision.

Declaration of Competing Interest

The authors declare that they have no known competing financial interests or personal relationships that could have appeared to influence the work reported in this paper.

Data availability

Data will be made available on request.

Acknowledgments

This work was supported by the Research Grants Council of the Hong Kong Special Administrative Region, China (PDFS2223-5S03 and PDFS2122-5S02) and the Hong Kong Polytechnic University (1-YY4A, 1-YWB6, and 1-ZE2F). B. Xu acknowledges the financial support from the Shenzhen Science and Technology Innovation Committee (Grant No. JCYJ20200109141014474).

Appendix A. Supporting information

Supplementary data associated with this article can be found in the online version at doi:10.1016/j.apcatb.2023.122710.

References

[1] C. Chen, Y. Kang, Z. Huo, Z. Zhu, W. Huang, H.L. Xin, J.D. Snyder, D. Li, J. A. Herron, M. Mavrikakis, M. Chi, K.L. More, Y. Li, N.M. Markovic, G.A. Somorjai, P. Yang, V.R. Stamenkovic, Highly crystalline multimetallic nanoframes with three-dimensional electrocatalytic surfaces, Science 343 (2014) 1339–1343.
[2] G. Feng, F. Ning, J. Song, H. Shang, K. Zhang, Z. Ding, P. Gao, W. Chu, D. Xia, Sub-2 nm ultrasmall high-entropy alloy nanoparticles for extremely superior electrocatalytic hydrogen evolution, J. Am. Chem. Soc. 143 (2021) 17117–17127.
[3] K. Huang, B. Zhang, J. Wu, T. Zhang, D. Peng, X. Cao, Z. Zhang, Z. Li, Y. Huang, Exploring the impact of atomic lattice deformation on oxygen evolution reactions based on a sub-5 nm pure face-centred cubic high-entropy alloy electrocatalyst, J. Mater. Chem. A 8 (2020) 11938–11947.
[4] G. Chen, Y. Zhu, H.M. Chen, Z. Hu, S.F. Hung, N. Ma, J. Dai, H.J. Lin, C.T. Chen, W. Zhou, Z. Shao, An amorphous nickel-iron-based electrocatalyst with unusual local structures for ultrafast oxygen evolution reaction, Adv. Mater. 31 (2019), e1900883.
[5] T. He, Y. Peng, Q. Li, J.E. Lu, Q. Liu, R. Mercado, Y. Chen, F. Nichols, Y. Zhang, S. Chen, Nanocomposites based on ruthenium nanoparticles supported on cobalt and nitrogen-codoped graphene nanosheets as bifunctional catalysts for electrochemical water splitting, ACS Appl. Mater. Interfaces 11 (2019) 46912–46919.
[6] Y. Zhu, G. Chen, Y.C. Chu, C.S. Hsu, J. Wang, C.W. Tung, H.M. Chen, Hetero-atomic pairs with a distal Fe^{3+}-site boost water oxidation, Angew. Chem. Int. Ed. Engl. (2022), e202211142.
[7] Y. Zhu, G. Chen, Y. Zhong, Y. Chen, N. Ma, W. Zhou, Z. Shao, A surface-modified antiperovskite as an electrocatalyst for water oxidation, Nat. Commun. 9 (2018) 2326.
[8] R.T. Hannagan, G. Giannakakis, M. Flytzani-Stephanopoulos, E.C.H. Sykes, Single-atom alloy catalysis, Chem. Rev. 120 (2020) 12044–12088.
[9] Y. Zhu, H.-C. Chen, C.-S. Hsu, T.-S. Lin, C.-J. Chang, S.-C. Chang, L.-D. Tsai, H. M. Chen, Operando unraveling of the structural and chemical stability of P-substituted $CoSe_2$ electrocatalysts toward hydrogen and oxygen evolution reactions in alkaline electrolyte, ACS Energy Lett. 4 (2019) 987–994.
[10] Y. Zhu, T.-R. Kuo, Y.-H. Li, M.-Y. Qi, G. Chen, J. Wang, Y.-J. Xu, H.M. Chen, Emerging dynamic structure of electrocatalysts unveiled by in situ x-ray diffraction/absorption spectroscopy, Energy Environ. Sci. 14 (2021) 1928–1958.
[11] K. Jiang, M. Luo, Z. Liu, M. Peng, D. Chen, Y.R. Lu, T.S. Chan, F.M.F. de Groot, Y. Tan, Rational strain engineering of single-atom ruthenium on nanoporous MoS_2 for highly efficient hydrogen evolution, Nat. Commun. 12 (2021) 1687.
[12] X. Kong, K. Xu, C. Zhang, J. Dai, S. Norooz Oliaee, L. Li, X. Zeng, C. Wu, Z. Peng, Free-standing two-dimensional Ru nanosheets with high activity toward water splitting, ACS Catal. 6 (2016) 1487–1492.
[13] B. Lu, L. Guo, F. Wu, Y. Peng, J.E. Lu, T.J. Smart, N. Wang, Y.Z. Finfrock, D. Morris, P. Zhang, N. Li, P. Gao, Y. Ping, S. Chen, Ruthenium atomically dispersed in carbon outperforms platinum toward hydrogen evolution in alkaline media, Nat. Commun. 10 (2019) 631.
[14] J. Mao, C.T. He, J. Pei, W. Chen, D. He, Y. He, Z. Zhuang, C. Chen, Q. Peng, D. Wang, Y. Li, Accelerating water dissociation kinetics by isolating cobalt atoms into ruthenium lattice, Nat. Commun. 9 (2018) 4958.
[15] Z. Peng, J. Liu, B. Hu, Y. Yang, Y. Guo, B. Li, L. Li, Z. Zhang, B. Cui, L. He, M. Du, Surface engineering on nickel-ruthenium nanoalloys attached defective carbon sites as superior bifunctional electrocatalysts for overall water splitting, ACS Appl. Mater. Interfaces 12 (2020) 13842–13851.

[16] J. Su, Y. Yang, G. Xia, J. Chen, P. Jiang, Q. Chen, Ruthenium-cobalt nanoalloys encapsulated in nitrogen-doped graphene as active electrocatalysts for producing hydrogen in alkaline media, Nat. Commun. 8 (2017) 14969.
[17] C. Wang, L. Qi, Heterostructured inter-doped ruthenium-cobalt oxide hollow nanosheet arrays for highly efficient overall water splitting, Angew. Chem. Int. Ed. Engl. 59 (2020) 17219–17224.
[18] L. Zhang, K. Xiong, S. Chen, L. Li, Z. Deng, Z. Wei, In situ growth of ruthenium oxide-nickel oxide nanorod arrays on nickel foam as a binder-free integrated cathode for hydrogen evolution, J. Power Sources 274 (2015) 114–120.
[19] L. Zhu, H. Zhang, W. Hu, J. Zheng, N. Zhang, C. Yu, H. Ye, Z. Yang, B.H. Chen, Nickel hydroxide-cobalt hydroxide nanoparticle supported ruthenium-nickel-cobalt islands as an efficient nanocatalyst for the hydrogenation reaction, ChemCatChem 10 (2018) 1998–2002.
[20] Y. Hu, G. Luo, L. Wang, X. Liu, Y. Qu, Y. Zhou, F. Zhou, Z. Li, Y. Li, T. Yao, Single Ru atoms stabilized by hybrid amorphous/crystalline FeCoNi layered double hydroxide for ultraefficient oxygen evolution, Adv. Energy Mater. 11 (2021), 2002816.
[21] T. Liu, J. Wang, C. Zhong, S. Lu, W. Yang, J. Liu, W. Hu, C.M. Li, Benchmarking three ruthenium phosphide phases for electrocatalysis of the hydrogen evolution reaction: experimental and theoretical insights, Chem. Eur. J. 25 (2019) 7826–7830.
[22] Y. Li, F. Chu, Y. Bu, Y. Kong, Y. Tao, X. Zhou, H. Yu, J. Yu, L. Tang, Y. Qin, Controllable fabrication of uniform ruthenium phosphide nanocrystals for the hydrogen evolution reaction, Chem. Commun. 55 (2019) 7828–7831.
[23] Z. Zhang, C. Jiang, P. Li, K. Yao, Z. Zhao, J. Fan, H. Li, H. Wang, Benchmarking phases of ruthenium dichalcogenides for electrocatalysis of hydrogen evolution: theoretical and experimental insights, Small 17 (2021), 2007333.
[24] Y. Jiao, Y. Zheng, K. Davey, S.-Z. Qiao, Activity origin and catalyst design principles for electrocatalytic hydrogen evolution on heteroatom-doped graphene, Nat. Energy 1 (2016) 16130.
[25] P.E. Blöchl, Projector augmented-wave method, Phys. Rev. B 50 (1994) 17953.
[26] W. Li, Y. Zhao, Y. Liu, M. Sun, G.I.N. Waterhouse, B. Huang, K. Zhang, T. Zhang, S. Lu, Exploiting Ru-induced lattice strain in CoRu nanoalloys for robust bifunctional hydrogen production, Angew. Chem. Int. Ed. Engl. 60 (2021) 3290–3298.
[27] Y. Qin, T. Yu, S. Deng, X.Y. Zhou, D. Lin, Q. Zhang, Z. Jin, D. Zhang, Y.B. He, H. J. Qiu, L. He, F. Kang, K. Li, T.Y. Zhang, RuO_2 electronic structure and lattice strain dual engineering for enhanced acidic oxygen evolution reaction performance, Nat. Commun. 13 (2022) 3784.
[28] L. Lin, Z. Sun, H. Yao, M. Yuan, H. Yang, H. Li, Q. Zhang, D. Wang, L. Gu, G. Sun, J. Zhu, W. Fang, Z. Tang, Tuning surface lattice strain toward a Pt-skin $CoPt_x$ truncated octahedron for hydrogen evolution reaction, J. Phys. Chem. C 123 (2019) 29722–29728.
[29] Y. Wang, X. Li, M. Zhang, Y. Zhou, D. Rao, C. Zhong, J. Zhang, X. Han, W. Hu, Y. Zhang, K. Zaghib, Y. Wang, Y. Deng, Lattice-strain engineering of homogeneous $NiS_{0.5}Se_{0.5}$ core-shell nanostructure as a highly efficient and robust electrocatalyst for overall water splitting, Adv. Mater. 32 (2020), e2000231.
[30] N. Cheng, S. Stambula, D. Wang, M.N. Banis, J. Liu, A. Riese, B. Xiao, R. Li, T. K. Sham, L.M. Liu, G.A. Botton, X. Sun, Platinum single-atom and cluster catalysis of the hydrogen evolution reaction, Nat. Commun. 7 (2016) 13638.
[31] J. Mahmood, F. Li, S.M. Jung, M.S. Okyay, I. Ahmad, S.J. Kim, N. Park, H.Y. Jeong, J.B. Baek, An efficient and pH-universal ruthenium-based catalyst for the hydrogen evolution reaction, Nat. Nanotechnol. 12 (2017) 441–446.
[32] A. Karmakar, S.S. Sankar, S. Kumaravel, R. Madhu, K.H. Mahmoud, Z.M. El-Bahy, S. Kundu, Ruthenium-doping-induced amorphization of VS_4 nanostructures with a rich sulfur vacancy for enhanced hydrogen evolution reaction in a neutral electrolyte medium, Inorg. Chem. 61 (2022) 1685–1696.
[33] J. Liu, Y. Zheng, D. Zhu, A. Vasileff, T. Ling, S.Z. Qiao, Identification of pH-dependent synergy on Ru/MoS_2 interface: a comparison of alkaline and acidic hydrogen evolution, Nanoscale 9 (2017) 16616–16621.
[34] N. Liu, Z. Zhai, B. Yu, W. Yang, G. Cheng, Z. Zhang, Bifunctional nanoporous ruthenium-nickel alloy nanowire electrocatalysts towards oxygen/hydrogen evolution reaction, Int. J. Hydrog. Energy 47 (2022) 31330–31341.
[35] C. Wei, X. Fan, X. Deng, L. Ma, X. Zhang, Q. Liu, J. Guo, Ruthenium doped Ni_2P nanosheet arrays for active hydrogen evolution in neutral and alkaline water, Sustain. Energy Fuels 4 (2020) 1883–1890.
[36] Y. Zheng, Y. Jiao, Y. Zhu, L.H. Li, Y. Han, Y. Chen, M. Jaroniec, S.Z. Qiao, High electrocatalytic hydrogen evolution activity of an anomalous ruthenium catalyst, J. Am. Chem. Soc. 138 (2016) 16174–16181.
[37] Y.R. Hong, S. Dutta, S.W. Jang, O.F. Ngome Okello, H. Im, S.Y. Choi, J.W. Han, I. S. Lee, Crystal facet-manipulated 2D Pt nanodendrites to achieve an intimate heterointerface for hydrogen evolution reactions, J. Am. Chem. Soc. 144 (2022) 9033–9043.
[38] Z.L. Wang, K. Sun, J. Henzie, X. Hao, C. Li, T. Takei, Y.M. Kang, Y. Yamauchi, Spatially confined assembly of monodisperse ruthenium nanoclusters in a hierarchically ordered carbon electrode for efficient hydrogen evolution, Angew. Chem. Int. Ed. Engl. 57 (2018) 5848–5852.
[39] L. Hu, J. Shi, Z. Peng, Z. Zheng, H. Dong, T. Wang, A high-density nickel-cobalt alloy embedded in nitrogen-doped carbon nanosheets for the hydrogen evolution reaction, Nanoscale 14 (2022) 6202–6211.
[40] M. Fang, Y. Ji, S. Geng, J. Su, Y. Li, Q. Shao, J. Lu, Metastable metal-alloy interface in RuNi nanoplates boosts highly efficient hydrogen electrocatalysis, ACS Appl. Nano Mater. 5 (2022) 17496–17502.
[41] J. Su, Y. Yang, G. Xia, J. Chen, P. Jiang, Q. Chen, Ruthenium-cobalt nanoalloys encapsulated in nitrogen-doped graphene as active electrocatalysts for producing hydrogen in alkaline media, Nat. Commun. 8 (2017) 14969.
[42] M. Yuan, C. Wang, Y. Wang, Y. Wang, X. Wang, Y. Du, General fabrication of RuM (M = Ni and Co) nanoclusters for boosting hydrogen evolution reaction electrocatalysis, Nanoscale 13 (2021) 13042–13047.
[43] Y. Zhu, J. Wang, H. Chu, Y.-C. Chu, H.M. Chen, In situ/operando studies for designing next-generation electrocatalysts, ACS Energy Lett. 5 (2020) 1281–1291.